Kent Academic Repository

Decoding the molecular complexity of the solar-type protostar NGC 1333 IRAS 4A

Heidy M. Quitián-Lara [1,2]★ Felipe Fantuzzi [1,3] Nigel J. Mason [1] and Heloisa M. Boechat-Roberty [2]

[1] *Centre for Astrophysics and Planetary Science, School of Physics and Astronomy, University of Kent, Park Wood Road, Canterbury CT2 7NH, UK*
[2] *Observatório do Valongo, Universidade Federal do Rio de Janeiro, Ladeira do Pedro Antônio 43, Rio de Janeiro 20080-090, Brazil*
[3] *School of Chemistry and Forensic Science, University of Kent, Park Wood Road, Canterbury CT2 7NH, UK*

ABSTRACT

The characterization of the molecular inventory of solar-type protostars is of crucial importance for a deep understanding of the chemical complexity underlying our cosmic origins. In this context, we present here the full millimetre line survey of the Class 0 protostellar object NGC 1333 IRAS 4A in the spectral bands at 3, 2, and 1.3 mm. In recognition of the powerful tool that unbiased spectral studies provide for investigating the chemistry and physics of star-forming regions, we provide a detailed description of the survey and the results of the analysis. We describe the identification of 1474 spectral lines belonging to 97 different molecular species, including complex organic molecules, which together cover the most ubiquitous chemical elements of life on Earth, namely carbon, hydrogen, nitrogen, oxygen, phosphorus, and sulphur. The abundances obtained herein are compared with the Class 0 protostellar objects L483 and L1527, and selected molecular ratios are used as tracers of physicochemical properties of the sources. Particularly, the dominance of oxygen-bearing species and the presence of distinct excitation temperature regimes support the attribution of NGC 1333 IRAS 4A as a hot corino featuring three physical components with distinguished and diverse chemical composition.

Key words: astrochemistry – stars: formation – ISM: abundances – ISM: jets and outflows – ISM: molecules.

1 INTRODUCTION

Compelling observational evidence, notably supported by isotopic studies, suggests that small celestial bodies within our Solar system, including comets and asteroids, have, to some extent, preserved the chemical composition from the early stages of the protosolar nebula (Pizzarello & Huang 2005; Cleeves et al. 2014). This retention may extend to the pre-stellar phase before the onset of gravitational collapse. Recently, the study of the composition of comet 67P/Churyumov–Gerasimenko (67P/C–G) by the *Rosetta* space mission has revealed the presence of numerous complex organic molecules (COMs). Some of these molecules are of pre-biotic and biological interests, including glycine (Altwegg et al. 2016, 2020; Schuhmann et al. 2019; Rivilla et al. 2020). Additionally, a comparative analysis with the relative abundances of CHO-, N-, and S-bearing molecules measured with the Atacama Large Millimeter/submillimeter Array (ALMA) towards the low-mass protostar IRAS 16293−2422B (Drozdovskaya et al. 2019) has shown a convincing correlation between protostellar and cometary data. This suggests that the volatile composition of cometesimals and planetesimals may have been partially inherited from the pre-stellar and protostellar phases of evolution.

From this standpoint, our comprehension of the chemistry occurring within star-forming regions is continuously enriched by persistent endeavours to replicate it, employing a combination of interstellar medium (ISM) models based on laboratory experiments and computational simulations. None the less, the alignment of observed COM abundances with these simulations remains a challenging puzzle. It hinges on the intricate interplay of numerous mechanisms, such as gas-phase and grain-surface chemistry, photolysis, and radiolysis, which collectively give rise to a multifaceted array of COMs within star-forming regions (Jørgensen, Belloche & Garrod 2020).

Despite the element of arbitrariness in the widely accepted definition of COMs as proposed by Herbst & van Dishoeck (2009), i.e. any carbon-containing molecule with at least six atoms, it accurately reflects the fact that the number of atoms in the molecules discovered in the ISM is relatively modest compared to the macromolecules present on Earth. Around 30 per cent of the over 300 species detected in the ISM (McGuire 2022) are COMs, making them essential components of the chemical composition of the interstellar gas (for further details, see the Molecules in Space catalogue of the Cologne Database for Molecular Spectroscopy, CDMS[1]). Another indicator of the chemical complexity in the ISM is the detection of species with multiple heteroatoms, such as formamide (NH_2CHO; Rubin et al. 1971), isocyanic acid (HNCO) and its isomers (Snyder & Buhl 1972; Brünken et al. 2009; Marcelino et al. 2009), and ethanolamine ($NH_2CH_2CH_2OH$; Rivilla et al. 2021). The significance of these molecules is underscored by the extensive body of research en-

[1] https://cdms.astro.uni-koeln.de/classic/catalog

compassing past experiments in astrochemistry (e.g. Öberg 2016; Herczku et al. 2021), insights into future experiments (Fulvio et al. 2021; Mason et al. 2021; Elsaesser et al. 2023), and advances in computational astrochemistry (Biczysko, Bloino & Puzzarini 2018; Sandford et al. 2020; Enrique-Romero et al. 2022; Germain et al. 2022). Particularly, there is a growing interest in exploring systems based on heavier main group atoms, such as sulphur (Laas & Caselli 2019; Bilalbegović et al. 2021; Mifsud et al. 2021) and phosphorus (Chantzos et al. 2020; Oliveira et al. 2020; Baptista & de Almeida 2023), spurred by recent astrochemical observations of molecules featuring these elements.

In recent decades, systematic studies of dark and pre-stellar cores have revealed surprising complexity. Observations have unveiled a much richer chemistry than initially anticipated, surpassing the predictions of models. In addition to the high presence of hydrocarbon chains in these environments, COMs such as methanol (CH_3OH), methyl formate (CH_3OCHO, or $HCOOCH_3$), and dimethyl ether (CH_3OCH_3) are frequently detected in star-forming regions. Experimental evidence supports the idea that CH_3OH can readily form through the subsequent hydrogenation of CO on icy grain mantles at low temperatures (Watanabe & Kouchi 2002). However, the mechanisms responsible for the formation of COMs, whether in the gas phase or on the surface of grains, remain subjects of debate. To address this, new and improved theoretical models and experiments are currently under development to identify different synthesis routes and mechanisms. These efforts encompass variations in the gas phase and ice mantles that may operate at each stage of pre-stellar core formation (Zamirri et al. 2019; Sandford et al. 2020; Turner & Kaiser 2020; Ceccarelli et al. 2022).

Concurrently, the abundant molecular deuteration observed in pre-stellar cores and throughout the subsequent phases of protostellar evolution, particularly in the Class 0 and Class I stages, naturally raises questions about chemical inheritance during the star and disc formation process (Bacmann et al. 2003; Caselli & Ceccarelli 2012). Consequently, an overarching understanding of this evolutionary process and its intricacies remains elusive. The limited number of studies conducted on a handful of objects thus far has primarily concentrated on COMs (Bottinelli et al. 2004b, 2007; Taquet et al. 2015), with a focus on their properties on a small scale.

Detailed information on the large-scale environment of solar-type protostellar objects is essential to fully characterize and understand their chemical evolution. To address this need, the Astrochemical Surveys At IRAM (ASAI; Lefloch et al. 2018)[2] was initiated, with the aim of exploring the molecular complexity in the evolution of low-mass stars, spanning from the initial pre-stellar phase to the late-stage status of these sources. The data used in this study are derived from the openly accessible ASAI repository,[3] which offers fully reduced and calibrated spectra of 10 distinct young stellar objects.

In this work, we present an unbiased spectral line survey of the Class 0 protostellar core IRAS 4A (see Section 2), conducted using the 30 m radio telescope of the Institute for Millimetre Radio Astronomy (IRAM) and utilizing data retrieved from the ASAI data base (vide supra). The survey covers the spectral windows of 72–116, 126–174, and 200–276 GHz. The motivation behind selecting IRAS 4A as our target is twofold: (i) it stands out as the brightest protostellar source within the ASAI sample, and (ii) it serves as a template for astrochemical investigations related to solar-type star formation. Additionally, we aim to achieve a comprehensive understanding of the molecular composition of this source. The intricacies of chemical networks often involve numerous actors, sometimes originating from 'chemical families' different from the primary molecule of interest or study. Despite numerous individual studies focusing on IRAS 4A, we believe that a holistic perspective of its chemical composition is still required. Therefore, the objective of this article is to offer a comprehensive view of the chemical composition of this Class 0 protostellar core.

2 THE SOURCE

IRAS 4 is a multiple Class 0 protostellar system situated in the active star-forming region NGC 1333 within the Perseus molecular complex, at a distance of ∼260 pc (Schlafly et al. 2014). Discovered by Jennings et al. (1987) and subsequently confirmed by Sandell et al. (1991), IRAS 4 is one of the first Class 0 protostellar systems recognized, shortly after the discovery of IRAS 16293−2422 and VLA 1623 (Andre, Ward-Thompson & Barsony 1993). IRAS 4 comprises two primary components, separated by an angular distance of ∼30 arcsec (IRAS 4A and IRAS 4B; Sandell et al. 1991; Langer, Castets & Lefloch 1996), with a third component, IRAS 4C, identified later at a position ∼50 arcsec north-east of IRAS 4A (Rodriguez, Anglada & Curiel 1999; Smith et al. 2000).

IRAS 4A is a strongly embedded protostellar core featuring a distinct warm region and measuring slightly less than 200 au in total size (Maret et al. 2004). Spectral lines from IRAS 4 have revealed multiple gas and dust layers, including (i) an extended gas layer at ambient velocities, characterized by narrow and fairly bright line profiles (∼1–5 km s^{-1}; Lefloch et al. 1998b; Koumpia et al. 2016), and (ii) high-velocity wings with extended profiles associated with the IRAS 4 outflow (Blake et al. 1995; Langer et al. 1996; Lefloch et al. 1998b). Using the IRAM 30 m telescope, Bottinelli et al. (2004a) detected the presence of CH_3OCHO, CH_3CN, and HCOOH in IRAS 4A, leading to its classification as a hot corino, the second member of this class shortly after the discovery of IRAS 16293−2422 (Bottinelli et al. 2004b).

While previous (sub-)millimetre line studies of IRAS 4A have been conducted (Blake et al. 1995), they were limited by lower sensitivity in the spectral data compared to the capabilities offered by the new Eight MIxer Receiver (EMIR) on the IRAM 30 m telescope. The significant enhancement in receiver performance, coupled with their wide spectral band (4–8 GHz), served as the linchpin for justifying the ambitious ASAI project. One of the early outcomes of ASAI, of particular significance, is the discovery of the unexpected richness of the pre-stellar phase, exemplified by the core L1544 (Lattanzi et al. 2020; Bianchi et al. 2023). This underscores the essentiality of acquiring detailed information about the large-scale environment surrounding solar-type protostars, enabling us to characterize and comprehend their chemical evolution inherited from the pre-stellar phase, once protostellar accretion has commenced and outflow mass-loss phenomena are underway. Currently, large (sub-)millimetre interferometers such as the Northern Extended Millimeter Array (NOEMA) and ALMA are unveiling an increasing number of hot corinos (Belloche et al. 2020; Yang et al. 2021), primarily through the advent of unbiased surveys like Seeds of Life in Space (SOLIS,[4] Ceccarelli et al. 2017) and Fifty AU STudy of the chemistry in the disk/envelope systems of Solar-like protostars (FAUST,[5] Codella et al. 2021).

Millimetre interferometry observations showed that both IRAS 4A and IRAS 4B are multiple systems (Lay, Carlstrom & Hills 1995; Looney, Mundy & Welch 2000). The distance between the two components of IRAS 4A (4A1 and 4A2) is merely ~1.8 arcsec (Jørgensen et al. 2007; Karska et al. 2013). The IRAS 4A system has an estimated range of dust temperatures around components IRAS 4A1 and IRAS 4A2 between $T_d = 50$ and 200 K (López-Sepulcre et al. 2017), a massive and dense envelope surrounding the nascent stars of 5.6 M$_\odot$ and a bolometric luminosity of 9.1 L$_\odot$ (Karska et al. 2013; Sahu et al. 2019). These results indicate that the component IRAS 4A1 is more than three times brighter than its companion IRAS 4A2 (Looney et al. 2000; Jørgensen et al. 2007; Santangelo et al. 2015).

IRAM/PdBI interferometer observations, with a resolution of ~2 arcsec, by Taquet et al. (2015) confirmed the hot corino nature of IRAS 4A and allowed its initial chemical characterization. Later, Santangelo et al. (2015) and López-Sepulcre et al. (2017), using the interferometer observations of the Plateau de Bure Interferometer (PdBI) and ALMA with angular resolutions of ~0.5 and ~0.3 arcsec, respectively, confirmed the status of IRAS 4A2 as a hot corino by the detection of several COMs, including CH_3OCH_3, ethyl cyanide (C_2H_5CN), and glycolaldehyde ($CH_2(OH)CHO$). More recently, De Simone et al. (2020) reported the detection of CH_3OH emission towards IRAS 4A1 during observations at longer centimetre wavelengths with the Expanded Very Large Array (EVLA), confirming the presence of organics towards the protostar. Indeed, it is now established that IRAS 4A1, IRAS 4A2, and IRAS 4B are hot corinos.

IRAS 4A powers a bipolar molecular outflow, whose chemical richness has been demonstrated in several observational studies. Emission from the outflow has been detected in many molecular tracers, such as CO, CS, H_2O, HCO$^+$, and SiO (Lefloch et al. 1998a, b; Santangelo et al. 2014). Observations at higher angular resolution with NOEMA hint at a chemical differentiation between the outflows of IRAS 4A1 and IRAS 4A2, and suggest that the IRAS 4A1 outflow is younger (De Simone et al. 2020).

Recent observations suggest that the southern filament in the Perseus/NGC 1333 region, where the IRAS 4A1, IRAS 4A2, and IRAS 4B protostars lie, may have been shaped by a collision between an expanding bubble and NGC 1333 (De Simone et al. 2022a). Dhabal et al. (2019) proposed that this collision could have led to the formation of the protostars, while De Simone et al. (2022b), based on observed abundance ratios and astrochemical models, suggested that it triggered a sudden collapse in a region where pre-collapse cores were not previously detected.

In Section 4, we provide a comprehensive overview of the extensive chemical composition of the Class 0 protostellar object NGC 1333 IRAS 4A. We categorize the various identified species into distinct elemental groups, thereby emphasizing the intricate nature of the chemical content observed in the aforementioned source.

3 OBSERVATIONS AND DATA REDUCTION

A full description of the observing strategy can be found in the general article presenting the Large Programme ASAI (Lefloch et al. 2018). Briefly, observations towards the nominal position of IRAS 4A [$\alpha_{(2000)} = 03^h29^m10^s.42$, $\delta_{(2000)} = +31°13'32.2''$] were carried out by the ASAI team over six semesters from 2012 September to 2015 March with the IRAM 30 m telescope. The broad-band EMIR receivers E090, E150, and E230 were used to cover the three spectral windows at 3, 2, and 1.3 mm, respectively. They were connected to fast Fourier transform spectrometers operating at their low (200 kHz) spectral resolution modes. Observations in the 3 mm (80–116 GHz)

and 2 mm (126–174 GHz) bands were performed simultaneously. The 1.3 mm band in the 200–276 GHz range was covered by simultaneous observations of the lower sideband and the upper sideband. Complementary observations of the 72–80 GHz band were obtained in 2016 January. The frequency of the local oscillator (LO) was regularly shifted by a fixed amount of 50 MHz. The half-power beamwidth (HPBW) of the IRAM 30 m radio telescope is described with quite accuracy by HPBW (arcsec) $= 2460/\nu$ (GHz). For ASAI observations, the typical beamwidth is in the range 21–34, 14–19, and 9–12 arcsec at 3, 2, and 1.3 mm, respectively.

Contamination from the nearby reference position was observed towards IRAS 4A for the bright, extended emission lines of some tracers such as CO, HCO$^+$, and HCN. The corresponding spectral settings (only) in the 3 mm band were re-observed in position-switching mode with a reference position checked as emission-free. This mainly concerns the spectral intervals of 87–94 and 103–111 GHz.

Pointing was carefully checked every hour at the nearby continuum source 0333+321 and pointing corrections were always less than 3 arcsec, less than one-third of a beamwidth at 1.3 mm. Focus was monitored regularly before and after sunset and proved to be stable with only minor corrections.

The data reduction was performed using the GILDAS/CLASS software developed at IRAM.[6] First, a linear function (polynomial function of degree 1) was subtracted from each spectrum. Following this step, spectra exhibiting pronounced noise or evident calibration issues were excluded from further consideration. This assessment involved a comparison of each scan with its (50 MHz LO) frequency-shifted counterpart, which allowed spurious signals to be identified and removed from the image band. The resulting scans were then averaged to obtain the final spectral bands.

The full line survey is presented in Table S7 in the Supporting Information (SI) file. Fluxes are expressed in units of antenna temperature corrected for atmospheric attenuation and rearward losses (T_A^*). Overall, an excellent sensitivity in all three millimetre bands was achieved, with a final root mean square (rms) in the range of 2–5 mK (T_A^*) per interval of 1 km s^{-1}, depending on frequency. The calibration uncertainty is typically 10, 15, and 20 per cent at 3, 2, and 1.3 mm, respectively.

For radiative transfer modelling and derivation of the molecular line emission properties, line fluxes were expressed in main-beam temperature units, T_{mb}. To convert from T_A^* to T_{mb}, we divided the former by B_{eff}/F_{eff}, where B_{eff} is the main-beam efficiency and F_{eff} is the forward efficiency. The B_{eff} values were derived from the expression $B_{eff} = 0.863 \exp[-(\nu(GHz)/361^2)]$ (Agúndez et al. 2019), while F_{eff} varied from 0.95 to 0.92 depending on the line frequency, as taken from the IRAM webpage.[7]

4 RESULTS

4.1 Line identification

4.1.1 Statistics

Table 1 shows the identified molecular species, considering only the main isotopologues identified in the ASAI survey. The physical conditions of the species as obtained by treatment of the spectral line survey are presented in Tables S1–S6 in the SI. The complete

[6]http://www.iram.fr/IRAMFR/GILDAS
[7]https://publicwiki.iram.es/Iram30mEfficiencies

Table 1. List of the 49 molecular species (main isotopologues only) directly detected through our spectral survey in IRAS 4A. The species are organized by their total number of atoms.

2	3	4	5
CO	HCO	H_2CO	H_2CCO
CN	HCN	$HCNH^+$	HCOOH
CS	HNC	HCNO	H_2COH^+
SiO	HCO^+	HNCO	HC_3N
NO	CCH	HOCN	c-C_3H_2
SO^+	H_2S	c-C_3H	C_4H
SO	SO_2	l-C_3H	
NS	N_2H^+	CCCS	
NS^+	OCS	$HOCO^+$	
PN	CCS	H_2CS	
	HCS^+	HSCN	
6	7	8	9
CH_3OH	CH_3CHO	CH_3OCHO	C_2H_5OH
CH_3CN	CH_3CCH	$CH_2(OH)CHO$	CH_3OCH_3
NH_2CHO			
CH_3SH			
HCCCHO			

were identified, which were ascribed to 97 different molecular species. From our analysis, we found that 49 of these molecules correspond to main isotopologues, and the remaining 48 feature one or more of the following rare isotopologues: deuterium (D), ^{13}C, ^{18}O, ^{17}O, ^{15}N, ^{33}S, ^{34}S, and ^{29}Si. Notably, HCCNC, previously mentioned in Lefloch et al. (2018), has not been incorporated into the current catalogue. This omission stems from the fact that its line intensities fall short of meeting the minimum threshold of a signal-to-noise ratio of 3σ. Furthermore, all observed NH_3 lines in IRAS 4A (De Simone et al. 2022a) are located outside the spectral bands encompassed by our study, rendering them beyond our detection capabilities. However, it is important to highlight that NH_2D, an isotopologue of NH_3, was unequivocally identified in our survey, providing supporting evidence for the presence of NH_3 in IRAS 4A. A similar rationale applies to H_2O, which is also indirectly detected through the emission of HDO. Finally, we also report seven unidentified (U) lines (see Section 4.1.3 for more details).

4.1.2 Elemental groups

Table 2 presents the list of molecular species identified in the survey. As expected, they are associated with the most abundant elements in the gas phase: O, C, N, and S. Two species bearing less abundant elements were also detected: PN and SiO. To facilitate the discussion, we have classified the detected species into four elemental groups: Oxygen-containing species (O-bearing group), sulphur-containing species (S-bearing group), nitrogen-containing species (N-bearing group), and carbon-based chains and cyclic species (C-chains group). It is worth noting that some species have mixed characteristics and therefore fall into more than one group. An example is CCS, which belongs to both the S-bearing and C-chains groups.

Fig. 2 shows the spectral line density of the identified lines classified into four elemental groups in all the three millimetre

catalogue of all detected spectral lines of IRAS 4A is shown in Table S7 in the SI. Examples of spectral bands with the detected molecular species are shown in Fig. 1 to illustrate the richness of the full line survey. Molecular lines were identified and analysed using version 6.3 of the CASSIS software (Vastel et al. 2015). We used the CDMS (Endres et al. 2016) and the Jet Propulsion Laboratory (JPL) catalogues (Pickett et al. 1998). A line was considered detected if its peak intensity was equal to or higher than the 3σ rms noise level. Observational properties were obtained from single or multiple Gaussian fits to the line profiles. In total, 1474 rotational transitions

Figure 1. Molecular line emission detected in representative spectral bands: 85 000–85 500 and 86 500–87 000 MHz (top), 165 000–165 500 and 170 000–170 500 MHz (middle), and 251 000–251 500 and 251 500–252 000 MHz (bottom), towards IRAS 4A in the 3, 2, and 1.3 mm bands, respectively. The main lines, with intensities higher than 3σ, are identified. Intensities are expressed in units of antenna temperature, T_A^*. An unidentified band (U) at 165 002.1 MHz is also shown (see Section 4.1.3 for more details).

Table 2. Census of molecular species detected towards IRAS 4A with signal-to-noise ratio larger than 3σ. Note that species may appear several times.

O-bearing group				
CO	^{13}CO	C^{17}O	C^{18}O	^{13}C^{17}O
^{13}C^{18}O	NO	SiO	^{29}SiO	SO
SO$^+$	S^{18}O	^{33}SO	^{34}SO	HDO
HCO	HCO$^+$	DCO$^+$	H^{13}CO$^+$	HC^{17}O$^+$
HC^{18}O$^+$	OCS	O^{13}CS	OC^{34}S	SO$_2$
^{34}SO$_2$	H$_2$CO	HDCO	D$_2$CO	H$_2^{13}$CO
H$_2$C^{18}O	HCNO	HNCO	HOCN	DNCO
HOCO$^+$	H$_2$COH$^+$	H$_2$CCO	HCOOH	CH$_3$OH
CH$_2$DOH	^{13}CH$_3$OH	NH$_2$CHO	CH$_3$CHO	HCCCHO
CH$_3$OCHO	CH$_2$(OH)CHO	C$_2$H$_5$OH	CH$_3$OCH$_3$	
S-bearing group				
CS	^{13}CS	C^{33}S	C^{34}S	NS
NS$^+$	SO	SO$^+$	S^{18}O	^{33}SO
^{34}SO	H$_2$S	HDS	D$_2$S	H$_2^{33}$S
H$_2^{34}$S	HCS$^+$	CCS	OCS	O^{13}CS
OC^{34}S	SO$_2$	^{34}SO$_2$	H$_2$CS	HDCS
D$_2$CS	H$_2$C^{34}S	HSCN	CCCS	CH$_3$SH
N-bearing group				
CN	^{13}CN	NO	NS	NS$^+$
PN	HCN	DCN	H^{13}CN	HC^{15}N
HNC	DNC	HN^{13}C	H^{15}NC	N$_2$H$^+$
N$_2$D$^+$	^{15}NNH$^+$	N^{15}NH$^+$	HCNH$^+$	HCNO
HNCO	DNCO	HOCN	HSCN	NH$_2$D
HC$_3$N	DC$_3$N	CH$_3$CN	NH$_2$CHO	
C-chains group				
CCH	CCD	CCS	l-C$_3$H	c-C$_3$H
CCCS	c-C$_3$H$_2$	c-C$_3$HD	C$_4$H	HC$_3$N
DC$_3$N	H$_2$CCO	HCCCHO	CH$_3$CCH	

bands. The average spectral line density is around 19 spectral lines per 2 GHz bin in 3 and 2 mm bands, while it is around 16 in the 1.3 mm band. This is comparable to the typical spectral line densities observed in other low-mass protostellar surveys, such as IRAS 16293−2422 ($\sigma = 10$–20 lines per 2 GHz bin; see Caux et al. 2011).

In Fig. 3, we present the relative weights of the four elemental groups (including species featuring rare isotopologues) in terms of the number of identified lines, the number of identified species, and total integrated intensities detected in our survey (excluding CO in this last case). The O-bearing species clearly dominate in all these indicators, accounting for 55 per cent in both the number of lines and the total flux. Moreover, they are also the most abundant group in terms of the number of identified species, making up 40 per cent of the total, with S-bearing and N-bearing species following closely behind at 25 and 24 per cent each. C-chains are the least represented group in terms of the number of species, comprising only 11 per cent.

When it comes to the number of lines, S-bearing, N-bearing, and C-chains contribute 20, 14, and 11 per cent, respectively. Importantly, the relative importance of these groups remains consistent across all indicators: whether we consider the number of lines, number of species, or emitted line flux.

Table 2 provides further insight into the abundance of these elemental groups, revealing that the O-bearing group contains the highest number of identified species, with 49 belonging to this category. In comparison, the S-bearing and N-bearing groups contribute 30 and 29 species, respectively, while the C-chains group remains significantly less diverse, with only 14 species. These trends in the distribution of species across elemental groups align with

observations in related protostellar envelopes as reported in previous studies (Agúndez et al. 2019, 2021; Bianchi et al. 2019).

Regarding the distribution of rare isotopologues, the deuterated species are the most abundant with a total number of 17 detected species, followed by the carbon ^{13}C isotopologues with 11 identified species. Amongst the oxygen isotopologues, five species contain ^{18}O atoms and three contain ^{17}O atoms; the rare sulphur isotopologues ^{34}S and ^{33}S occur six and three times, respectively, in our census; and four species containing a ^{15}N atom and one species featuring ^{29}Si have been detected. It is worth mentioning that two species, ^{13}C^{17}O and ^{13}C^{18}O, each contain two rare isotopologues. Consequently, the total count here is 50, rather than 48, which is the sum of species featuring rare isotopologues.

Within each chemical group, we can also order the species and define the 'observationally dominant' species by comparing the total integrated flux emitted by the main isotopologues, as shown in Table 3. This comparison is merely indicative, since (i) the fluxes are proportional to the molecular abundances, but also depend on the excitation conditions, and (ii) for some species, especially the simplest ones, which have a small number of lines, some of them may fall within the frequency holes of our survey, so the total flux of the species may be significantly underestimated. For example, the HCO$^+$ transition $J = 2$–1 is not visible in our survey, despite having high probabilities and being in a medium that provides ideal excitation conditions for these transitions.

The total luminosity budget is largely dominated by CO (see Table 3) and the main contributor immediately after CO is CH$_3$OH. We found that only two species (H$_2$CO and SO) have a contribution equal to or higher than 50 per cent of the flux radiated by CH$_3$OH. This simple qualitative criterion indicates that the bulk of the radiated flux in the millimetre domain is actually dominated by only a few species.

O-bearing group: The line survey shows a remarkable dominance of O-bearing species, with 990 molecular lines identified. A large number of these lines are attributed to COMs, in particular, CH$_3$OH, CH$_3$CHO, CH$_3$OCHO, CH$_3$OCH$_3$, C$_2$H$_5$OH, and NH$_2$CHO. Chemically related species, such as H$_2$CO, HCOOH, and H$_2$CCO, as well as the C$_2$H$_4$O$_2$ isomers methyl formate (CH$_3$OCHO, or HCOOCH$_3$) and glycolaldehyde (CH$_2$(OH)CHO) were also detected. Furthermore, we have identified seven spectral lines tentatively associated with acetic acid (CH$_3$COOH), another C$_2$H$_4$O$_2$ isomer. The presence of CH$_3$COOH in NGC 1333 IRAS 4 has been previously reported by Remijan et al. (2003) in earlier studies of the source. However, the abundance estimated by us using both the rotational diagram (RD) analysis and the non-LTE excitation and radiative transfer RADEX code yielded inconsistent results when compared to those of its congeners. Consequently, we opted not to include this molecule in our catalogue. The high content of O-bearing COMs is a characteristic feature of hot corino sources and is consistent with the presence of a hot corino in IRAS 4A (Bottinelli et al. 2007; López-Sepulcre et al. 2017).

S-bearing group: Molecules featuring a sulphur atom constitute the second most abundant family in terms of molecular lines and radiated flux, just after the O-bearing group. The list of detected S-bearing species, which is given in Table 2, corresponds to a total of 368 molecular lines. Similar to the O-bearing group, S-bearing lines are continuously distributed over the entire spectral bands. Most of the detected S-bearing species are two- or three-atom molecules. Two S-bearing carbon chains, CCS and CCCS, have also been detected. The radiated flux is dominated by SO and CS, but H$_2$CS and SO$_2$ also contribute significantly (about 20 per cent of the maximum flux). Finally, we also detected the first as yet only S-bearing COM: CH$_3$SH.
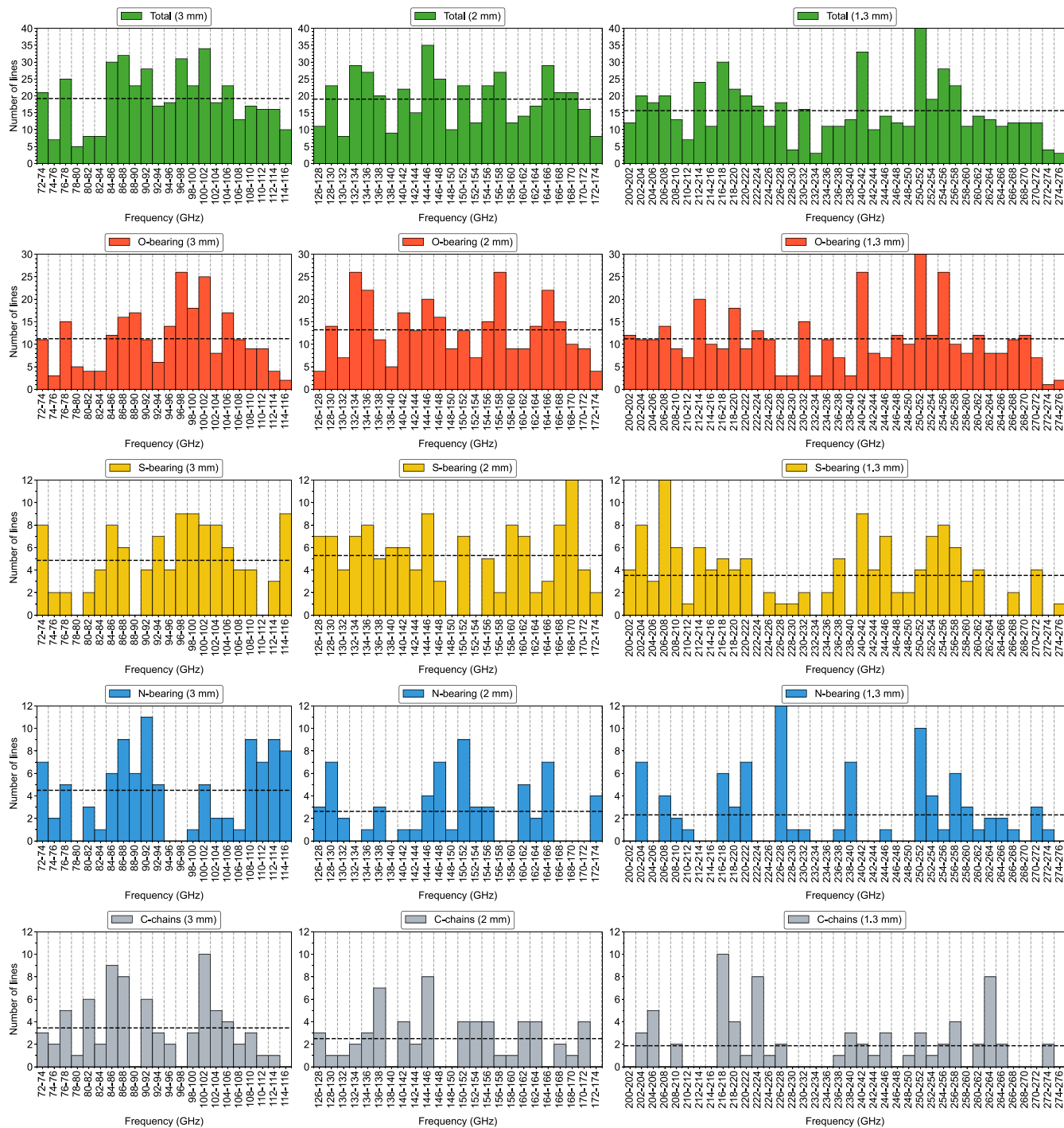
Figure 2. Spectral line density distribution (averaged over 2 GHz bins) in each of the three spectral bands of the survey as a function of the elemental group. The horizontal dashed lines show the average values of the line density of each group in the three spectral bands. The following counts are observed at or above the maximum values of their corresponding y-scales: Total (1.3 mm, 250–252 GHz) with 51 lines, O-bearing (1.3 mm, 250–252 GHz) with 47 lines, S-bearing (2 mm, 168–170 GHz) with 13 lines, S-bearing (1.3 mm, 206–208 GHz) with 12 lines, and N-bearing (1.3 mm, 226–228 GHz) with 13 lines.

N-bearing group: In the IRAS 4A spectral line survey, we identified a total of 250 lines of N-bearing species. These molecules rank third in terms of identified lines, while the number of species detected is very similar to that of S-bearing species. In terms of flux, the emission is dominated by HCN, followed by HNC, but N_2H^+, CN, HC_3N, and CH_3CN contribute to the flux to a similar extent. In

our survey, we could only detect two N-bearing COMs: CH_3CN and NH_2CHO.

C-chains group: Most of the hydrocarbons detected in IRAS 4A are highly unsaturated linear chains and therefore exhibit a high C/H ratio. The total number of molecular lines identified in this group is 207. The most dominant species in terms of flux is HC_3N, but five
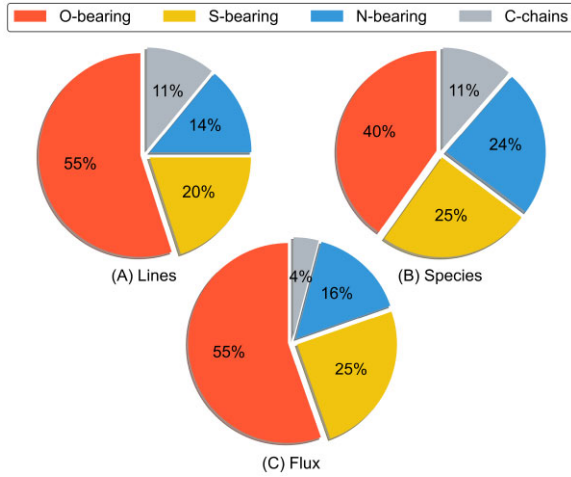
Figure 3. Relative contributions (per cent) of the different elemental groups in IRAS 4A for (A) number of lines, (B) number of species, and (C) collected flux of all molecules except CO.

other species show contributions greater than 30 per cent of the HC_3N flux. The linear molecules CCH, $l\text{-}C_3H$, and C_4H are identified in the source. However, higher order polyynes, containing five or more carbon atoms, were not detected in our survey. We also observe the presence of the cyclic C-bearing molecules $c\text{-}C_3H$ and $c\text{-}C_3H_2$, the former being a structural isomer of $l\text{-}C_3H$. The $c\text{-}C_3H_2$ species is even the second flux contributor in this group. As previously mentioned, small chains containing two or three C atoms with S or N atoms incorporated were also detected. Lastly, the unsaturated hydrocarbon propyne (or methyl acetylene, CH_3CCH) is also identified. This is the only C-chain-bearing COM (following the definition of Herbst & van Dishoeck 2009) identified in the survey.

Table 4. Frequency and observational parameters (linewidth expressed in FWHM, flux and peak flux expressed in T_A^*) of the unidentified lines of the spectral survey. Frequencies were estimated by adopting a rest velocity of $v = 7$ km s^{-1}. Only detections with a signal-to-noise ratio larger than 5σ are reported. The observational parameters were obtained from a simple Gaussian fit to the line profile. The uncertainties are given in brackets. Velocity-integrated fluxes and line intensities are expressed in units of antenna temperature corrected for atmospheric attenuation.

Rest frequency (MHz)	FWHM (km s^{-1})	Flux (mK km s^{-1})	T_A^* (mK)
73 367.7	2.4 (0.5)	41.0 (7.5)	22.9 (3.3)
85 294.8	1.2 (0.3)	20.0 (4.0)	16.0 (2.9)
90 669.8	1.6 (0.3)	18.0 (3.0)	11.0 (1.8)
112 563.3	1.8 (0.4)	40.0 (8.0)	21.1 (5.7)
165 002.1	1.4 (0.1)	216.1 (12.3)	65.9 (5.8)
165 273.7	1.7 (0.3)	9.1 (7.1)	19.7 (2.5)
249 591.7	2.5 (0.2)	92.2 (5.4)	30.6 (2.2)

4.1.3 Unidentified lines

Out of the 1474 lines identified in our survey, 7 lines detected at a signal-to-noise ratio better than 5σ could not be assigned a spectroscopic identification. These *unidentified* molecular lines are listed in Table 4; the frequencies are given assuming a source velocity of 7 km s^{-1}. The analysis of our spectral line survey reveals some scatter in the line emission peak velocities, as discussed in Section 4.3, so the frequency accuracy is of the order of 200 kHz (0.6 km s^{-1}) in the 3 mm band. A comparison with the other spectral line surveys may help to better characterize the frequency of these 'U' lines and hopefully determine their spectroscopic properties.

In the course of the IRAS 4A survey analysis, we were able to identify and characterize lines previously labelled as U lines in Lefloch et al. (2018). This advancement follows the discovery of new molecular signatures within the millimetre range. Notably, the lines at 100 198.47 and 150 295.61 MHz (see Table S7 in the SI) have been attributed to the $J = 2\text{–}1$ and $J = 3\text{–}2$ rotational transitions

Table 3. Main isotopologues of the four elemental groups, ordered by decreasing total flux (K km s^{-1}). The flux is expressed in terms of T_{mb}. The CO flux given here is estimated from the observed ^{13}CO flux (12 K km s^{-1}) multiplied by the elemental $^{12}C/^{13}C$ abundance ratio of 68 (Milam, Woolf & Ziurys 2009). Only species with a total flux value above 0.50 K km s^{-1} are shown. For a complete version of this table with all species, including those featuring rare isotopologues, see Table S6 in the SI.

O-bearing group			S-bearing group			N-bearing group			C-chains group		
Species	No. of lines	Flux	Species	No. of lines	Flux	Species	No. of lines	Flux	Species	No. of lines	Flux
CO	2	797	SO	28	90	HCN	7	52	HC_3N	27	10
CH_3OH	223	178	CS	6	58	HNC	4	15	$c\text{-}C_3H_2$	29	7.6
H_2CO	26	102	H_2CS	37	18	CN	21	12	CH_3CCH	36	4.9
SO	28	90	SO_2	49	17	N_2H^+	3	11	H_2CCO	36	4.4
SO_2	49	17	OCS	21	9.2	HC_3N	27	10	CCH	10	3.7
CH_3CHO	122	13	H_2S	4	8.6	CH_3CN	60	8.8	CCS	22	3.4
HCO^+	2	11	NS	21	4.1	NS	21	4.1	HCCCHO	3	2.4
OCS	21	9.2	CCS	22	3.4	HNCO	10	2.9			
$C^{18}O$	2	8.1	HCS^+	7	1.2	NO	17	2.7			
CH_3OCHO	108	5.3	SO^+	7	0.79						
H_2CCO	36	4.4									
HNCO	10	2.9									
SiO	3	2.9									
NO	17	2.7									
HCCCHO	3	2.4									
CH_3OCH_3	23	1.6									
SO^+	7	0.79									
HCOOH	15	0.73									

of the NS$^+$ cation (Cernicharo et al. 2018). Furthermore, we have now identified the U line at 91 359.0 MHz in Lefloch et al. (2018), as corresponding to D$_2$S (91 359.12 MHz; Camy-Peyret et al. 1985; see Table S7 in the SI). These identifications only became possible by comparing unbiased spectral surveys of the molecular line emission in the different millimetre windows with laboratory experiments.

One of these unattributed lines merits in-depth scrutiny, namely the one characterized by a rest frequency of 165 002.1 MHz. This specific line distinguishes itself as the most intense amongst its unidentified peers, exhibiting a radiative flux of 216.1 mK km s^{-1}. A search into the JPL data base (Pickett et al. 1998) has provided support for the hypothesis that this particular line could be associated with 1,3-propanediol (C$_3$H$_8$O$_2$). Regrettably, our current survey has produced an insufficient quantity of spectral lines tentatively associated with this molecule, preventing us from reaching a definitive conclusion regarding its presence in IRAS 4A. To date, only two diol-containing molecules have been identified within the ISM: ethylene glycol, (CH$_2$OH)$_2$, and (Z)-1,2-ethenediol, (CHOH)$_2$. Ethylene glycol was initially detected in emission towards the Galactic Centre source Sagittarius B2(N-LMH) through the resolution of several millimetre-wave rotational torsional transitions pertaining to its lowest energy conformer (Hollis et al. 2002). In turn, (Z)-1,2-ethenediol, the enol form of glycolaldehyde, was observed in the G+0.693-0.027 molecular cloud situated in the Galactic Centre and is considered a key molecular precursor of the ribonucleic acid (RNA) world (Rivilla et al. 2022).

Experimental investigations have shed light on the possibility of 1,3-propanediol formation within methanol ices when exposed to ionizing radiation at 10 K, simulating radiation doses equivalent to those experienced by interstellar ices over the extended lifespan of enduring molecular clouds, of a few 10^7 yr (Zhu et al. 2020). Furthermore, it is noteworthy that molecular ions featuring diol moieties manifest as the lowest energy C$_2$H$_4$O$_2^+$ isomers, including as the global minimum structure (Fantuzzi et al. 2011, 2012). This observation holds particular importance, as neutral C$_2$H$_4$O$_2$ isomers are ubiquitously encountered within the ISM (Burke et al. 2015; Ahmad et al. 2020).

Based on our present findings, we have opted to retain the 165 002.1 MHz line as an unidentified spectral feature. However, we strongly endorse the need for further explorations, especially considering the multitude of pertinent facets associated with the 1,3-propanediol molecule, which may serve as a plausible source of this spectral signature.

4.2 Line kinematics

The identified lines were fitted by Gaussian profiles. All line profiles identified in this survey exhibit a narrow component with a linewidth [full width at half-maximum (FWHM)] of 1–3 km s^{-1}. In each of the other elemental groups, with the exception of the C-chains group, where this feature is absent, a second, broad velocity component with a typical FWHM value ranging between 4 and 12 km s^{-1} was detected in a small number of species. The list of detected species and their physical properties are given in Table S5 in the SI.

Fig. 4 shows a compilation of selected line profiles that are representative of the four elemental groups and their Gaussian fits. The wide component could usually be fitted by one single Gaussian profile, except for SiO. In this case, the wide emission was modelled by two distinct Gaussian components on each side of the narrow central emission. To further address and discuss the interpretation of the narrow and wide components, we selected species from each chemical group that have both narrow and broad components or

only narrow components and present lines over a wide range of line upper level energy (E_{up}) values to investigate the possible variations of the kinematic parameters with the E_{up} values of the lines. Fig. 5 shows the observational properties (linewidth and peak velocity) of the CH$_3$OH, HC$_3$N, H$_2$CS, and CH$_3$CCH lines respectively for the O-bearing, N-bearing, S-bearing, and C-chains groups.

4.2.1 The narrow component

All four chemical groups share the same properties (see Tables S1–S4 in the SI): the line velocities are very close to 7 km s^{-1} [see Fig. 5, with very small dispersion (somewhat larger for CH$_3$OH as discussed below)], and no evidence of a peak velocity gradient as a function of E_{up}, which could trace infall motions inside the envelope. The linewidths also show little dispersion and are close to 2 km s^{-1}. There is an obvious decrease in linewidths with increasing E_{up}, which is particularly visible for HC$_3$N, a linear molecule for which the E_{up} and frequency scales are perfectly proportional. This behaviour simply reflects the more limited velocity resolution for the low-frequency spectra.

As explained in more detail in Section 5.1, the quiescent gas associated with the narrow component traces the cold protostellar envelope of the system.

4.2.2 The wide component

The Gaussian fits for the wide components are more uncertain than those for the narrow ones, partly because the wide emission is weaker than the narrow, especially at low E_{up} values, and probably also because the Gaussian shape is a less representative line-shape model for the wide component. Thus, for all three species showing wide emission in Fig. 5, the kinematic properties of the wide components show a larger dispersion than those of the narrow components, especially at low E_{up}. However, common tendencies can be observed: The central velocities of the lines show a slight gradient from about 5 km s^{-1} at $E_{up} \simeq 20$ K to about 7 km s^{-1} at $E_{up} \simeq 70$ K and above. The linewidths exhibit a very similar behaviour, with a decrease from about 10 km s^{-1} at $E_{up} \simeq 20$ K to about 6 km s^{-1} at $E_{up} \simeq 70$ K and above.

Fig. 5 also shows that the line profiles and the linewidths of the wide component differ depending on the molecular species. It can be seen that the CH$_3$OH lines, which are very numerous, show much larger dispersion in central velocities and linewidths than the other species. At least two features of the CH$_3$OH spectrum contribute to this dispersion: (i) the CH$_3$OH spectrum is very dense and many lines partially overlap, so the uncertainties of the Gaussian fits are larger compared to isolated lines, and (ii) the lines corresponding to a given E_{up} interval may belong to large frequency ranges, so they may have very different spectral resolutions expressed in velocity units. Using single-dish telescopes, several groups have mapped the distribution of this spatially extended wide component in the millimetre transitions of molecular tracers such as e.g. SiO or CS, and they showed that it traces actually the signature of the outflows powered by the protostellar system (for further details, see Section 2).

4.3 Line excitation

4.3.1 Methodology

The excitation conditions of each molecular species (gas column density and excitation temperature) were determined from a population diagram analysis of the spectral line emission in the approximation
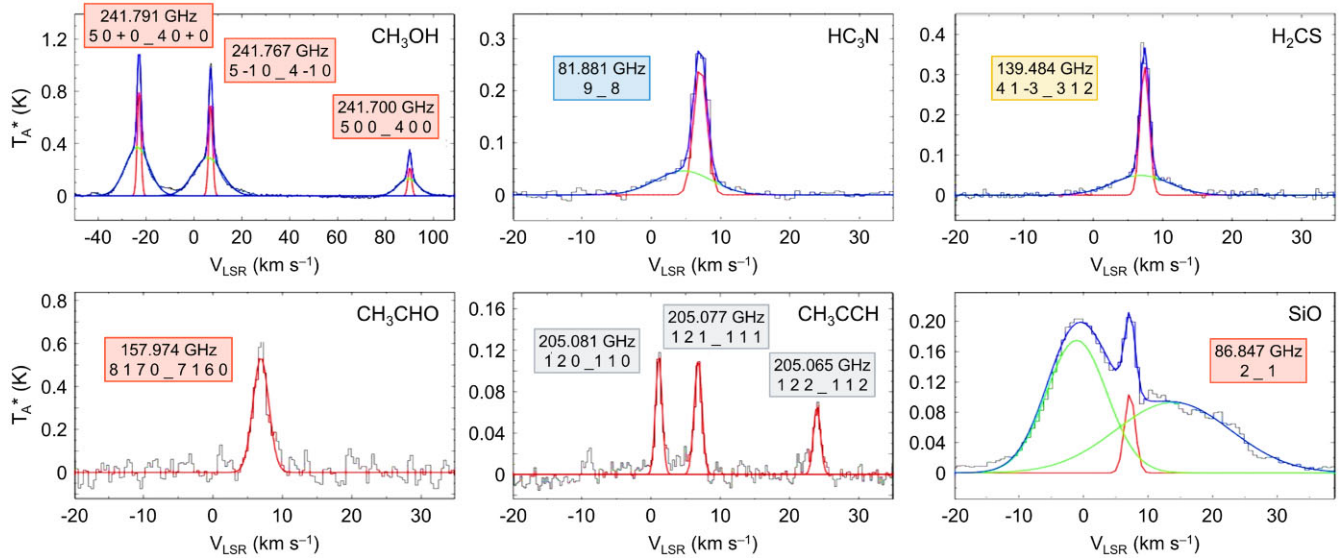
Figure 4. Gaussian fits of selected spectral lines, expressed as T_A^* per velocity of local standard of rest, V_{LSR}, representative of the four elemental groups. In the plots, narrow components are depicted in red, wide components in green, and when both are present, the total fit is displayed in blue. For the SiO line, two Gaussian components are required to accurately reproduce the wide emission. The inset boxes display the frequency lines and their corresponding line quantum numbers as sourced from the CDMS and JPL catalogues. For the full IRAS 4A catalogue as obtained herein, see Table S7 in the SI.

of local thermodynamic equilibrium (LTE) using the CASSIS code (Vastel et al. 2014). Examples of typical RDs illustrating the various cases encountered are displayed in Fig. 6. We did not apply any main-beam filling factor correction to the line fluxes, which were expressed in main-beam temperature units. In other words, the emission is assumed to be extended and to fill in the IRAM 30 m beam. Therefore, the obtained gas column densities are all main-beam averaged.

The narrow and wide components were analysed separately. The best-fitting values and uncertainties for column density and rotational temperature are reported in Table S5 in the SI for the wide component and Tables S1–S4 in the SI, for the narrow component. The E- and A-types of species such as CH_3OH and CH_3CN were not separated. We used the same procedure for *ortho-* and *para-* forms of a molecular species, such as H_2CS or H_2S, although it clearly leads to a bias if only one transition of an *ortho-* or *para-* form is detected. This is illustrated by H_2S, whose population diagram analysis based on two transitions (one *ortho-* and one *para-*) yields a T_{ex} of $\sim$47 K; in contrast, a much lower value of $\sim$11 K is found for the deuterated isotopologue HDS. In the case of species with only one detected transition and/or species with a hyperfine structure (e.g. N_2H^+, assuming $T = 15$ K), a simple LTE fit was performed.

4.3.2 The wide component

The wide component observed within each elemental group exhibits fairly homogeneous excitation properties, with moderate excitation temperatures between 20 and 40 K. However, we can note that CH_3OH also exhibits the presence of a second, wide-warm component, with excitation temperatures around 80 K, as shown in Fig. 6 and Table S5 in the SI.

4.3.3 The narrow component

As illustrated in Tables S1–S4 in the SI, roughly 80 per cent of the molecular species can be fitted by a single component

of 'low' excitation temperature, typically below 40 K. However, certain species, such as H_2CS, HC_3N, H_2CO, and OCS, display a second, higher excitation component. Notably, a subset of species such as CH_3OH, CH_3CN, and CH_3OCHO exhibit three distinct excitation components: cold, warm, and hot, respectively. These three components are detected in approximately similar ranges of E_{up} for the different molecular species: below 40 K for the cold component, between 40 and 150 K for the warm component, and above 150 K for the hot one. However, it is important to acknowledge that the range of energy levels (E_{up}) covered by our observations varies across different molecular species, as evident from the distinct x-axis ranges in Fig. 5. Consequently, the presence of warm and hot components cannot be equally explored for all species, given the variability in available data.

It is rather tempting to associate the warm and the hot components with the inner region of the envelope, heated up by the protostars, where the gas kinetic temperature gradually increases to cause the sublimation of the ice grains and the release of their material into the gas phase, as evidenced by the detection of HDO (Table S1 in the SI; also Coutens et al. 2013) and COMs on a small scale in the protostellar system (Taquet et al. 2015; López-Sepulcre et al. 2017). We exclude a significant contribution of outflow shocks (see Santangelo et al. 2014; De Simone et al. 2020) as the spectral signatures display narrow linewidths.

5 DISCUSSION

In this section, we discuss the identification of the physical nature of the cold, warm, and hot components of IRAS 4A based on the kinematics of the detected spectral lines and the excitation conditions. Our survey reveals a rich chemical content in both components, which allows not only a detailed comparison between them but also a comparison with predictions from chemical models. In this article, we focus on the former comparison, while the latter is outside our current goals.
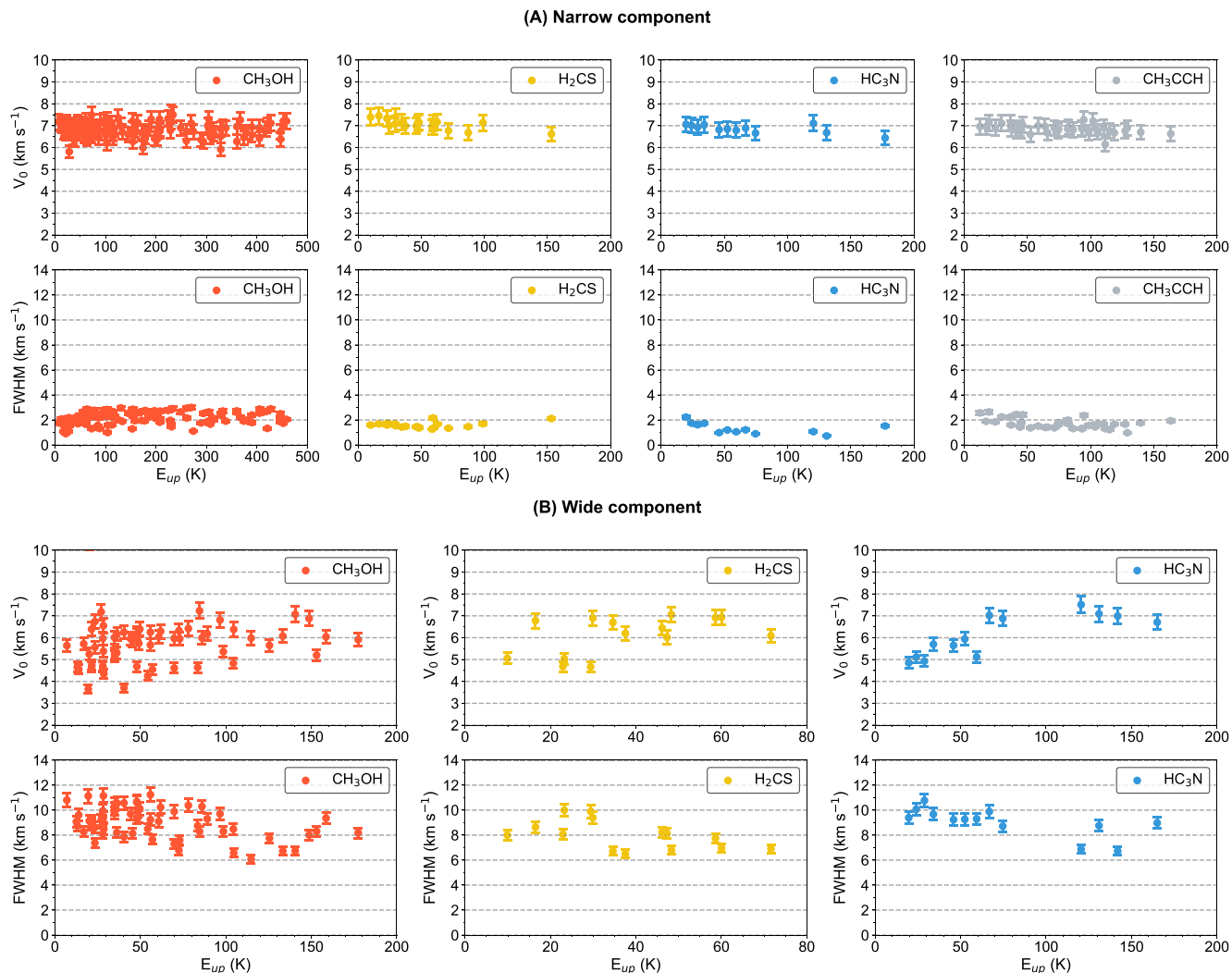
(A) Narrow component

(B) Wide component

Figure 5. Central velocities (V_0) and widths (FWHM) of the (A) narrow and (B) wide Gaussian components, as a function of E_{up}, of representative species of the four elemental groups.

5.1 The cold component

We have labelled the low-excited gas component 'cold' because the T_{ex} of the molecular species are as low as 7 K and usually less than 40 K. The majority of molecular species have been detected in this domain, in contrast to the less frequent detections associated with the 'warm' (moderately excited) and 'hot' (highly excited) components, which are herein discussed together as 'warm + hot' whenever appropriate. Many observational arguments unambiguously point to a low gas kinetic temperature. We list some of them below:

(i) The HCN/HNC abundance ratio is well known to be sensitive to the gas kinetic temperature (Hacar, Bosman & van Dishoeck 2020). Here, the H^{13}CN/HN^{13}C ratio is close to 1, indicating that the kinetic temperature of the emitting gas is low, similar to that of pre-stellar and cold dark cores, whereas it increases by one to two orders of magnitude in warm protostellar environments (Hirota et al. 1998). It is worth mentioning, however, that our results suggest that the opacity of HCN and possibly H^{13}CN transitions is not negligible (vide infra).

(ii) A large number of singly deuterated species are detected in the four elemental families. We also note the detection of *doubly* deuterated formaldehyde (D$_2$CO) and thioformaldehyde (D$_2$CS). Early studies by Parise et al. (2002) reported the detection of doubly deuterated methanol.

(iii) The molecular ion N$_2$H$^+$ is easily destroyed by CO in the gas phase through N$_2$H$^+$ + CO → N$_2$ + HCO$^+$. Hence, the detection of N$_2$H$^+$ is an indication that CO is actually depleted from the gas on to the dust grains. The CO depletion on to dust grains is well documented by observations and requires a gas kinetic temperature below 20 K (Caselli et al. 1999; Bacmann et al. 2002; Aikawa 2008; Cazaux et al. 2017).

These arguments clearly demonstrate that the component featuring low-excitation gas indeed consists of gas with a low kinetic temperature. Together with the quiescent kinematics of this component, we conclude that the molecular emission originates from the cold protostellar envelope, detected at large by millimetre continuum observations (see e.g. Lefloch et al. 1998a). Based on the continuum map of the region published by these authors, and the LTE-RADEX model of HCO$^+$, we have estimated a typical H$_2$ column density of about $N_{H_2} \sim 1.0 \times 10^{22}$ cm^{-2}.

As previously anticipated, we have also detected a phosphorus-containing species in IRAS 4A, namely PN, with line characteristics
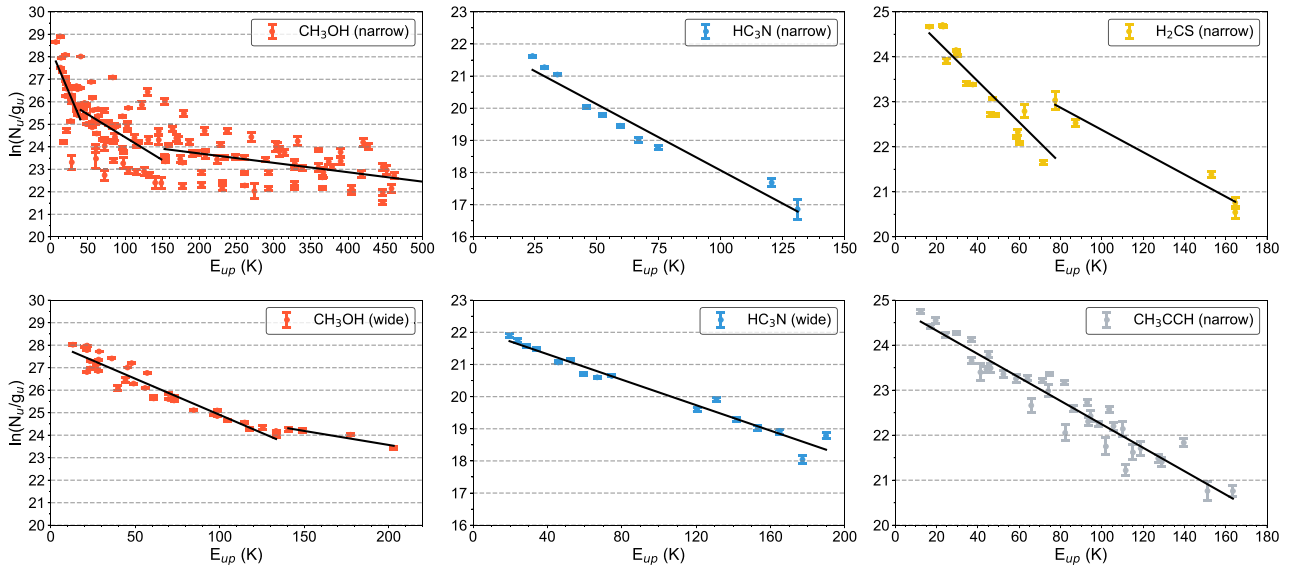
Figure 6. Typical RDs illustrating the various cases encountered in the radiative transfer modelling of the molecular line emission in IRAS 4A: CH$_3$OH (three narrow components: cold, warm, and hot; two wide components: cold and warm), HC$_3$N (one narrow component; one wide component), H$_2$CS (two narrow components: cold and warm), and CH$_3$CCH (one narrow component).

consistent with the cold envelope, i.e. narrow linewidths and low excitation temperature. This discovery is puzzling as phosphorus is thought to be strongly depleted on to dust, and so far, P-bearing species have been detected only towards shocks in low- (Lefloch et al. 2016) and high-mass (Mininni et al. 2018; Fontani et al. 2019; Rivilla et al. 2020) star-forming regions. Clearly, the origin of this emission and the reaction pathway of PN formation require further investigation by modellers and observers.

5.2 Comparison of the cold component in different objects

Here, we compare the IRAS 4A molecular abundances (relative to H$_2$) of selected species with those obtained from other Class 0 protostars (see Table 5), namely L483 and L1527.

L483 is a dense core located in the Serpens-Aquila Rift star-forming region at about ∼200 pc [$\alpha_{(2000)} = 18^\mathrm{h}17^\mathrm{m}29\overset{s}{.}947$ and $\delta_{(2000)} = -04°39'39\overset{''}{.}55$; Dame & Thaddeus 1985; Okoda et al. 2021]. This dense core is a significant astrochemical site, housing important molecular species such as HCCO, HCS, HSC, and CNCN, which were first identified by Agúndez, Cernicharo & Guélin (2015) and Agúndez et al. (2018, 2019). Using ALMA observations, Oya et al. (2017) and Jacobsen et al. (2019) detected compact emissions of COMs within a less than 100 au, characteristic of hot corinos, indicating that L483 exhibits a dual nature with traits of both warm carbon-chain chemistry (WCCC) and hot corino chemistry. Probably, this dual chemistry is a result of L483 undergoing gravitational collapse, in transition from Class 0 to Class I, as indicated by the line profiles of molecules such as H$_2$CO and CS, with a characteristic signature of infall motions, including pronounced self-absorption at higher redshifted velocities (Tafalla et al. 2000).

L1527 is a dark cloud in the Taurus molecular complex at ∼140 pc [$\alpha_{(2000)} = 04^\mathrm{h}39^\mathrm{m}53\overset{s}{.}9$ and $\delta_{(2000)} = +26°03'09\overset{''}{.}6$; Tobin et al. 2008]. L1527 houses the Class 0 low-mass protostar IRAS 04368+2557, known as a prototypical WCCC source (Sakai et al. 2008, 2010; Sakai & Yamamoto 2013). Previous works reported on the infalling motion of the envelope gas while conserving angular momentum, based on interferometer observations (Ohashi et al. 1997; Yen et al.

Table 5. Comparison of molecular abundances (relative to H$_2$) in the low-excitation gas component of IRAS 4A with the Class 0 protostars L483 and L1527, taken from Agúndez et al. (2019) and Yoshida et al. (2019).

	L483	L1527	IRAS 4A
N_{H_2} (cm^{-2})	4.0×10^{22}	8.2×10^{22}	1.0×10^{22}
HCO	7.0×10^{-11}	9.0×10^{-11}	2.0×10^{-10}
HCO$^+$	1.7×10^{-10}	3.8×10^{-9}	1.0×10^{-9}
H$_2$CO	1.4×10^{-9}	1.9×10^{-9}	2.2×10^{-9}
CH$_3$OH	7.6×10^{-9}	2.8×10^{-10}	1.2×10^{-8}
CH$_3$CHO	9.5×10^{-11}	2.0×10^{-11}	9.5×10^{-10}
SO	5.0×10^{-9}	1.3×10^{-10}	8.8×10^{-10}
H$_2$CS	3.5×10^{-10}	3.5×10^{-11}	9.4×10^{-10}
CS	5.8×10^{-10}	4.2×10^{-10}	2.5×10^{-9}
CCS	1.2×10^{-10}	7.0×10^{-11}	2.8×10^{-10}
NH$_2$D	1.8×10^{-9}	1.8×10^{-11}	5.0×10^{-9}
CN	1.7×10^{-9}	3.2×10^{-9}	3.9×10^{-9}
HCN^a	6.0×10^{-10}	8.0×10^{-10}	2.5×10^{-9}
HNC	2.0×10^{-10}	1.4×10^{-9}	2.8×10^{-9}
HNCO	4.3×10^{-10}	3.2×10^{-11}	3.8×10^{-10}
C$_2$H	1.3×10^{-8}	1.9×10^{-8}	4.4×10^{-9}
C$_4$H	3.0×10^{-9}	2.8×10^{-9}	4.6×10^{-10}
c-C$_3$H	2.0×10^{-10}	1.7×10^{-10}	1.3×10^{-10}
c-C$_3$H$_2$	5.3×10^{-9}	5.3×10^{-10}	3.1×10^{-10}
CH$_3$CCH	2.3×10^{-9}	8.5×10^{-10}	2.5×10^{-9}

^{a}Abundance of IRAS 4A estimated from the LTE-RADEX fit using CASSIS software.

2013). The chemical composition of the protostar changes according to the kinematic characteristic inside the rotating envelope in the disc formation. Observational and modelling evidence suggests that gas accretion in this source undergoes significant chemical processing, including gas-grain interactions in the transition zone (Sakai et al. 2014a, b; Oya et al. 2015).

Considering only the species identified in the low-excitation region of each object, we start our discussion with the O-bearing group, which contains the majority of COMs. Within this group, it is worth noting a similarity in the abundance of simple molecules. Amongst

the COMs, all species are more abundant in IRAS 4A. In the case of CH$_3$OH (1.2×10^{-8} in IRAS 4A), the difference exceeds the abundance in L483 in about twice times (7.6×10^{-9}) and in L1527 (2.8×10^{-10}) around two orders of magnitude higher. Although the origin and efficiencies of these species in cold, dense clouds are not entirely clear, it is known that these species can form naturally in dust grains from CO adsorption followed by multiple hydrogenation steps (Watanabe & Kouchi 2002; Minissale et al. 2016). On the other hand, for CH$_3$CCH (IRAS 4A: 2.5×10^{-9}), the difference decreases, with very similar abundances in L483 (2.3×10^{-9}) and three times higher in L1527 (8.5×10^{-10}). This species, as a component of the carbon chains, emphasizes that even within the context of the molecular species within that group, IRAS 4A exhibits a comparable molecular abundance.

This introduces us to the next group, the C-chains. As mentioned above, almost all species have similar abundances in all sources. However, the abundance of C$_2$H (4.4×10^{-9}) and C$_4$H (4.6×10^{-10}) are at least three times and at least six times lower in IRAS 4A, compared to the abundances in L483 (1.3×10^{-8}; 3.0×10^{-9}) and L1527 (1.9×10^{-8}; 2.8×10^{-9}), respectively. Given that a higher abundance of carbon chains typically indicates an earlier evolutionary stage, we analysed the C$_2$H/C$_4$H ratio, revealing that the smallest value corresponds to that of L483 (C$_2$H/C$_4$H $\sim$4), followed by L1527 (C$_2$H/C$_4$H $\sim$7), and IRAS 4A (C$_2$H/C$_4$H $\sim$10). These values suggest that the C$_2$H/C$_4$H ratio could be used as a tracer of molecular evolution, with higher values indicating more evolved sources. Furthermore, an attempt to correlate between C-chains and COMs shows that a high C$_2$H/CH$_3$OH ratio is characteristic of WCCC sources, while lower values correspond to hot corino (Taniguchi, Gorai & Tan 2023). The C$_2$H/CH$_3$OH ratios for L483 ($\sim$2), IRAS 4A ($\sim$0.4), and L1527 ($\sim$68) are consistent with those documented in the literature. These ratios provide an important indicator of the dual nature of L483, illustrating its characteristics as both a WCCC source and a hot corino.

In the N-bearing group, we observe that the HCN abundance in IRAS 4A (2.5×10^{-9}) is almost four times higher than that of L483 (6.0×10^{-10}) and three times higher than that of L1527 (8.0×10^{-10}). We also observe that HCN has a similar abundance to that of its isotope HNC (2.8×10^{-9}) in IRAS 4A, with HCN/HNC $\sim$0.9. This value is greater than that of L1527 ($\sim$0.6), but is lower than that of L483 ($\sim$3). Considering that the HCN/HNC ratio is temperature sensitive (Schilke et al. 1992; Hacar et al. 2020), this value is expected to be $\sim$1 (Sarrasin et al. 2010) for cold molecular clouds and to increase directly proportional to the object temperature, a property that standard astrochemical models cannot reproduce (Graninger et al. 2014; Koumpia et al. 2016). Additionally, we note that the HCN abundance in IRAS 4A (2.5×10^{-9}) is similar to that of CN (3.9×10^{-9}), while the abundance of CN in IRAS 4A (for comparison, L483: 1.7×10^{-9}; L1527: 3.2×10^{-9}) is 6.5 times that of HCN in L483 (6.0×10^{-10}), and around five times that of L1527 (8.0×10^{-10}). These results suggest that the opacity of the transitions of HCN, CN, and their isotopologues are probably not negligible, as previously anticipated. Taking these results into account, we can rank the sources according to their corresponding temperatures, with the coldest object being L1527, followed by IRAS 4A, and the warmest being L483. This result is consistent with the differences in the bolometric luminosity of the sources, where L483 presents the highest value of $L_\odot = 13$, followed by IRAS 4A $L_\odot = 9$, and finally L1527 $L_\odot = 1.7$ (Oya et al. 2017; Lefloch et al. 2018).

Concerning the deuterated species NH$_2$D, its relative abundance in IRAS 4A (5.0×10^{-9}) is two orders of magnitude higher than in L1527 (1.8×10^{-11}), and around three times higher than that of L483 (1.8×10^{-9}). Deuterated molecules, especially those featuring nitrogen atoms, are selective tracers of the cooler, denser gas in molecular clouds and star-forming cores, due to the depletion of C-bearing molecules (van Dishoeck & Blake 1998; Roberts & Millar 2007; Friesen et al. 2018).

Finally, we compare the abundance of S-bearing species in the mentioned objects. Comparing the SO/CS ratio, an indicator that can be used as a chemical clock or tracer of the source's transition state from a pre-stellar nucleus to a protostar (Bergin & Langer 1997; Kontinen et al. 2000; Esplugues et al. 2023), we observe that L483 presents the highest value with SO/CS $\sim$9, while L1527 and IRAS 4A have an SO/CS $\sim$0.3. These results suggest that L483 is the most evolved source in our sample. Indeed, substantial variations in the relative abundance of the molecules depicted in Table 5, particularly those belonging to the S-bearing and C-chains groups, are observed. This suggests that these molecules are potential evolutionary tracers of protostellar objects.

5.3 The high-excitation gas

Next, we have attempted to confirm that the warm-hot gas is in fact tracing the hot corino environment. To achieve this, we employed the abundances derived from IRAM 30 m radio telescope observations and applied the RD analysis, accounting for beam dilution effects. We compared selected molecular species to those derived from two other sets of observations: the PdBI observations of IRAS 4A with a 2 arcsec angular resolution by Taquet et al. (2015) and the ALMA observations with a 0.5 arcsec angular resolution by López-Sepulcre et al. (2017).

We have assumed a total gas column density of $N_{H_2} = 1.0 \times 10^{25}$ cm^{-2}, while using a source size of 0.3 arcsec. The reference to this hot corino size is grounded in a comparison of abundances derived from observations conducted with the IRAM 30 m telescope and those obtained from interferometer observations. Additionally, the choice of $N_{H_2} = 1.0 \times 10^{25}$ cm^{-2} for IRAS 4A represents an averaged value, drawing from data reported by Taquet et al. (2015) (3.7×10^{25} cm^{-2}) and López-Sepulcre et al. (2017) [$(2.9–16) \times 10^{24}$ cm^{-2}]. This ensures an appropriate representative value for comparison. Both the PdBI and ALMA data were analysed using the RD method, which involves averaging column densities over the source size. We made the assumption that the H$_2$ column density remains constant within the beam. Furthermore, beam dilution effects were taken into account during our RD analysis.

When comparing the column densities of selected species, including COMs (as shown in Table 6), derived from the warm-hot component of the IRAM 30 m data to those from the interferometric data, we observed a striking level of consistency. Notably, our observations revealed that the relative abundances obtained in various observations, whether from ALMA, PdBI, or IRAM 30 m, consistently displayed similar column densities, typically falling within a factor of 2. This consistency holds regardless of whether we assume the source to be extended (100 arcsec) or with a size of 0.3 arcsec in the case of the IRAM 30 m observations. These results provide compelling evidence that the warm-hot excitation component, as identified through the IRAM 30 m radio telescope, indeed traces the hot corino region.

5.4 Chemical distribution

In Fig. 7, we compare the distribution of the different elemental groups (by number of species) in the cold and warm + hot regions of IRAS 4A based on the kinematics of the spectral lines and excitation

Table 6. Comparison of the abundances (relative to H_2) of selected molecules (including COMs) in the high-excitation component of IRAS 4A with IRAM 30 m and those obtained by interferometric observations. Abundances are taken from Taquet et al. (2015) with PdBI and López-Sepulcre et al. (2017) with ALMA. See text for details.

	IRAM 30 m	PdBI	ALMA
Source size (arcsec)	0.3	0.5	0.3
N_{H_2} (cm^{-2})	1.0×10^{25}	3.7×10^{25}	$(2.9-16) \times 10^{24}$
H_2CO	10×10^{-8}		
CH_3OH	1.8×10^{-8}	1.7×10^{-8}	
H_2CCO	2.9×10^{-9}	4.2×10^{-10}	
CH_3CHO	9.5×10^{-10}		$(11-74) \times 10^{-10}$
C_2H_5OH	4.0×10^{-9}	1.2×10^{-9}	$(4-19) \times 10^{-9}$
CH_3OCH_3	5.6×10^{-9}	8.5×10^{-10}	$(9-11) \times 10^{-9}$
HCOOH	8.7×10^{-10}		$(6-29) \times 10^{-10}$
CH_3OCHO	6.4×10^{-9}		
CH_3CN	3.8×10^{-10}	1.8×10^{-10}	$(4-21) \times 10^{-9}$
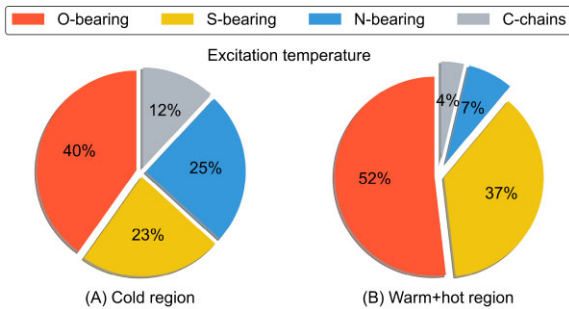
Figure 7. Distribution of elemental group contributions by the number of species (per cent) in both cold and warm + hot regions of IRAS 4A (see Tables S1–S4 in the SI).

conditions. Our study reveals a rich chemical content in the two components, both of which are clearly dominated by O-bearing group species. In this group, 14 of the 47 O-bearing species are found in the warm + hot region, and most of these belong to the main isotopologues. Surprisingly, only CH_3OH, OCS, and their isotopologues $^{13}CH_3OH$, CH_2DOH, $O^{13}CS$, and $OC^{34}S$ are found simultaneously in both cold and warm + hot regions of IRAS 4A. Similarly, we also observe a significant change in the distribution of S-bearing species in the two components. In this case, its contribution becomes severely dominant over the N-bearing and C-chains groups in the warm + hot component, where 10 S-bearing molecular species are identified. In stark contrast, only two N-bearing species (NH_2D and CH_3CN) and one belonging to the C-chains group (H_2CCO) are identified in the higher excitation component. It is worth mentioning that H_2CCO also belongs to the O-bearing group, so no polyynic chain, open chain, or cyclic species featuring only hydrogen and carbon atoms are identified in the warm + hot component of IRAS 4A. Taken together, these results provide solid evidence that the distinct physical components of IRAS 4A have a distinguished and diverse chemical composition and distribution.

5.5 The wide component

The wide component emission shows kinematic characteristics in good agreement with those observed for the outflow emission (Lefloch et al. 1998a, b; Santangelo et al. 2014, 2015). The bipolar nature of this outflow is particularly evident in the SiO profile shown in Fig. 4. The gradients observed for the lines' central velocities

and linewidths (see Section 4.2) are also indicative of the outflow nature of this component. Finally, the chemical composition of this component, in which SiO emission is particularly strong and in which the S-bearing species are very abundant, also suggests the existence of shocks.

Recent observations with higher angular resolution (and sensitivity) with the NOEMA interferometer by De Simone et al. (2020) in the framework of the Large Programme SOLIS (Ceccarelli et al. 2017) have revealed the presence of several shocks from the IRAS 4A outflows in the central region of ~20 arcsec radius around the protostars IRAS 4A1 and IRAS 4A2, which is therefore approximately covered by the IRAM 30 m beam in the 3 mm spectral window. Although the SOLIS line survey clearly established the chemical activity of the IRAS 4A outflow (Taquet et al. 2020), the only COM detected in the outflow was CH_3OH, along with ketene (H_2CCO) as a COM-related organic species. In comparison, De Simone et al. (2020) was able to map the emission of rotational transitions from several COMs, such as acetaldehyde (CH_3CHO), dimethyl ether (CH_3OCH_3), and formamide (NH_2CHO), thanks to the much higher sensitivity of the NOEMA interferometer.

6 CONCLUSIONS

In this work, we have analysed the full ASAI spectral line survey of NGC 1333 IRAS 4A, carried out between 72 and 276 GHz with the IRAM 30 m telescope, using the CASSIS software. We have detected 97 molecular species, including rare isotopologues, and identified a grand total of 1474 rotational transitions, including narrow and wide components. We confirm the molecular richness previously reported by the ASAI team (Lefloch et al. 2018). The spectrum is dominated by the emission of O-bearing molecular species, a characteristic feature of a hot corino. In addition, S-bearing and N-bearing species are also found to be very abundant.

The analysis of the ASAI survey of IRAS 4A has allowed us to obtain a chemical and physical description of the protostellar envelope. Using the kinematic properties of the spectral lines and the RD analysis, we have highlighted three components in the molecular emission:

(i) A component rich in simple molecular species with narrow lines (linewidths of the order of 2 km s^{-1} or below), particularly abundant in carbon-based chains and cyclic species, and excitation temperatures below ~40 K. We assign this component to the cold outer envelope.

(ii) A warm + hot excitation component, also with narrow lines, but with temperatures ranging from ~40 to more than 150 K. This component displays a rich content in COMs, which is consistent with hot corinos surrounding the embedded protostellar sources as observed at subarcsec resolution with the NOEMA and ALMA interferometers.

(iii) A broad line component (linewidths of the order of 6 km s^{-1} or above) with moderate excitation (between ~20 and 40 K), showing strong SiO emission and numerous S-bearing species. We conclude that this component corresponds to the outflow powered by the protostellar system.

The richness of our study in terms of molecular content certainly deserves further analysis, in particular a possible separation of the chemical contents of the warm + hot component. A detailed analysis of the S-bearing species and C-chains offers potential pieces of evidence in terms of chemical evolution during the protostar formation process and in relation to outflow conditions. We therefore hope that further studies can be presented in the forthcoming period.

ACKNOWLEDGEMENTS

DATA AVAILABILITY

Data are available on request.

REFERENCES

Agúndez M., Cernicharo J., Guélin M., 2015, A&A, 577, L5

Agúndez M., Marcelino N., Cernicharo J., Tafalla M., 2018, A&A, 611, L1

Agúndez M., Marcelino N., Cernicharo J., Roueff E., Tafalla M., 2019, A&A, 625, A147

Agúndez M., Marcelino N., Tercero B., Cabezas C., de Vicente P., Cernicharo J., 2021, A&A, 649, L4

Ahmad A., Shivani, Misra A., Tandon P., 2020, Res. Astron. Astrophys., 20, 014

Aikawa Y., 2008, Astrophys. Space Sci., 313, 35

Altwegg K. et al., 2016, Sci. Adv., 2, e1600285

Altwegg K. et al., 2020, Nat. Astron., 4, 533

Andre P., Ward-Thompson D., Barsony M., 1993, ApJ, 406, 122

Bacmann A., Lefloch B., Ceccarelli C., Castets A., Steinacker J., Loinard L., 2002, A&A, 389, L6

Bacmann A., Lefloch B., Ceccarelli C., Steinacker J., Castets A., Loinard L., 2003, ApJ, 585, L55

Baptista L., de Almeida A. A., 2023, J. Phys. Chem. A, 127, 1000

Belloche A. et al., 2020, A&A, 635, A198

Bergin E. A., Langer W. D., 1997, ApJ, 486, 316

Bianchi E. et al., 2019, MNRAS, 483, 1850

Bianchi E. et al., 2023, ApJ, 944, 208

Biczysko M., Bloino J., Puzzarini C., 2018, WIREs Comput. Mol. Sci., 8, e1349

Bilalbegović G., Maksimović A., Valencic L. A., Lehtola S., 2021, ACS Earth Space Chem., 5, 436

Blake G. A., Sandell G., van Dishoeck E. F., Groesbeck T. D., Mundy L. G., Aspin C., 1995, ApJ, 441, 689

Bottinelli S. et al., 2004a, ApJ, 615, 354

Bottinelli S. et al., 2004b, ApJ, 617, L69

Bottinelli S., Ceccarelli C., Williams J. P., Lefloch B., 2007, A&A, 463, 601

Brünken S., Gottlieb C. A., McCarthy M. C., Thaddeus P., 2009, ApJ, 697, 880

Burke D. J., Puletti F., Brown W. A., Woods P. M., Viti S., Slater B., 2015, MNRAS, 447, 1444

Camy-Peyret C., Flaud J.-M., Lechuga-Fossat L., Johns J., 1985, J. Mol. Spectrosc., 109, 300

Caselli P., Ceccarelli C., 2012, A&AR, 20, 56

Caselli P., Walmsley C. M., Tafalla M., Dore L., Myers P. C., 1999, ApJ, 523, L165

Caux E. et al., 2011, A&A, 532, A23

Cazaux S., Martín-Doménech R., Chen Y. J., Caro G. M. M., Díaz C. G., 2017, ApJ, 849, 80

Ceccarelli C. et al., 2017, ApJ, 850, 176

Ceccarelli C. et al., 2022, preprint (arXiv:2206.13270)

Cernicharo J. et al., 2018, ApJ, 853, L22

Chantzos J., Rivilla V. M., Vasyunin A., Redaelli E., Bizzocchi L., Fontani F., Caselli P., 2020, A&A, 633, A54

Cleeves L. I., Bergin E. A., Alexander C. M. O., Du F., Graninger D., Oberg K. I., Harries T. J., 2014, Science, 345, 1590

Codella C., Ceccarelli C., Chandler C., Sakai N., Yamamoto S., Team FAUST, 2021, Front. Astron. Space Sci., 8, 782006

Coutens A. et al., 2013, A&A, 560, A39

Dame T. M., Thaddeus P., 1985, ApJ, 297, 751

De Simone M. et al., 2020, A&A, 640, A75

De Simone M. et al., 2022a, MNRAS, 512, 5214

De Simone M. et al., 2022b, ApJ, 935, L14

Dhabal A., Mundy L. G., Chen C.-y., Teuben P., Storm S., 2019, ApJ, 876, 108

Drozdovskaya M. N., van Dishoeck E. F., Rubin M., Jørgensen J. K., Altwegg K., 2019, MNRAS, 490, 50

Elsaesser A. et al., 2023, npj Microgravity, 9, 43

Endres C. P., Schlemmer S., Schilke P., Stutzki J., Müller H. S., 2016, J. Mol. Spectrosc., 327, 95

Enrique-Romero J., Rimola A., Ceccarelli C., Ugliengo P., Balucani N., Skouteris D., 2022, ApJS, 259, 39

Esplugues G. et al., 2023, A&A, 678, A199

Fantuzzi F., Pilling S., Santos A. C. F., Baptista L., Rocha A. B., Boechat-Roberty H. M., 2011, MNRAS, 417, 2631

Fantuzzi F., Baptista L., Rocha A. B., Boechat-Roberty H. M., 2012, Int. J. Quantum Chem., 112, 3303

Fontani F., Rivilla V. M., van der Tak F. F. S., Mininni C., Beltrán M. T., Caselli P., 2019, MNRAS, 489, 4530

Friesen R. K., Beltrán M. T., Caselli P., Garrod R. T., 2018, preprint (arXiv:1810.07163)

Fulvio D., Potapov A., He J., Henning T., 2021, Life, 11, 568

Germain A., Tinacci L., Pantaleone S., Ceccarelli C., Ugliengo P., 2022, ACS Earth Space Chem., 6, 1286

Graninger D. M., Herbst E., Öberg K. I., Vasyunin A. I., 2014, ApJ, 787, 74

Hacar A., Bosman A. D., van Dishoeck E. F., 2020, A&A, 635, A4

Herbst E., van Dishoeck E. F., 2009, ARA&A, 47, 427

Herczku P. et al., 2021, Rev. Sci. Instrum., 92, 084501

Hirota T., Yamamoto S., Mikami H., Ohishi M., 1998, ApJ, 503, 717

Hollis J. M., Lovas F. J., Jewell P. R., Coudert L. H., 2002, ApJ, 571, L59

Jacobsen S. K., Jørgensen J. K., Di Francesco J., Evans N. J., Choi M., Lee J.-E., 2019, A&A, 629, A29

Jennings R. E., Cameron D. H. M., Cudlip W., Hirst C. J., 1987, MNRAS, 226, 461

Jørgensen J. K. et al., 2007, ApJ, 659, 479

Jørgensen J. K., Belloche A., Garrod R. T., 2020, ARA&A, 58, 727

Karska A. et al., 2013, A&A, 552, A141

Kontinen S., Harju J., Heikkila A., Haikala L. K., 2000, A&A, 361, 704

Koumpia E., van der Tak F. F. S., Kwon W., Tobin J. J., Fuller G. A., Plume R., 2016, A&A, 595, A51

Laas J. C., Caselli P., 2019, A&A, 624, A108

Langer W. D., Castets A., Lefloch B., 1996, ApJ, 471, L111

Lattanzi V., Bizzocchi L., Vasyunin A. I., Harju J., Giuliano B. M., Vastel C., Caselli P., 2020, A&A, 633, A118

Lay O. P., Carlstrom J. E., Hills R. E., 1995, ApJ, 452, L73

Lefloch B., Castets A., Cernicharo J., Langer W. D., Zylka R., 1998a, A&A, 334, 269

Lefloch B., Castets A., Cernicharo J., Loinard L., 1998b, ApJ, 504, L109

Lefloch B. et al., 2016, MNRAS, 462, 3937

Lefloch B. et al., 2018, MNRAS, 477, 4792

Looney L. W., Mundy L. G., Welch W. J., 2000, ApJ, 529, 477

López-Sepulcre A. et al., 2017, A&A, 606, A121

McGuire B. A., 2022, ApJS, 259, 30

Marcelino N., Cernicharo J., Tercero B., Roueff E., 2009, ApJ, 690, L27

Maret S. et al., 2004, A&A, 416, 577

Mason N. J., Hailey P. A., Mifsud D. V., Urquhart J. S., 2021, Front. Astron. Space Sci., 8, 739046

Mifsud D. V. et al., 2021, Space Sci. Rev., 217, 14

Milam S. N., Woolf N. J., Ziurys L. M., 2009, ApJ, 690, 837

Mininni C., Fontani F., Rivilla V. M., Beltrán M. T., Caselli P., Vasyunin A., 2018, MNRAS, 476, L39

Minissale M., Moudens A., Baouche S., Chaabouni H., Dulieu F., 2016, MNRAS, 458, 2953

Öberg K. I., 2016, Chem. Rev., 116, 9631

Ohashi N., Hayashi M., Ho P. T. P., Momose M., 1997, ApJ, 475, 211

Okoda Y., Oya Y., Abe S., Komaki A., Watanabe Y., Yamamoto S., 2021, ApJ, 923, 168

Oliveira R. R., Molpeceres G., Fantuzzi F., Quitián-Lara H. M., Boechat-Roberty H. M., Kästner J., 2020, MNRAS, 500, 2564

Oya Y., Sakai N., Lefloch B., López-Sepulcre A., Watanabe Y., Ceccarelli C., Yamamoto S., 2015, ApJ, 812, 59

Oya Y. et al., 2017, ApJ, 837, 174

Parise B. et al., 2002, A&A, 393, L49

Pickett H., Poynter R., Cohen E., Delitsky M., Pearson J., Müller H., 1998, J. Quant. Spectrosc. Radiat. Transfer, 60, 883

Pizzarello S., Huang Y., 2005, Geochim. Cosmochim. Acta, 69, 599

Remijan A., Snyder L. E., Friedel D. N., Liu S., Shah R. Y., 2003, ApJ, 590, 314

Rivilla V. M. et al., 2020, MNRAS, 492, 1180

Rivilla V. M. et al., 2021, Proc. Natl. Acad. Sci., 118, e2101314118

Rivilla V. M. et al., 2022, ApJ, 929, L11

Roberts H., Millar T. J., 2007, A&A, 471, 849

Rodriguez L. F., Anglada G., Curiel S., 1999, ApJS, 125, 427

Rubin R. H., Swenson G. W. J., Benson R. C., Tigelaar H. L., Flygare W. H., 1971, ApJ, 169, L39

Sahu D., Liu S.-Y., Su Y.-N., Li Z.-Y., Lee C.-F., Hirano N., Takakuwa S., 2019, ApJ, 872, 196

Sakai N., Yamamoto S., 2013, Chem. Rev., 113, 8981

Sakai N., Sakai T., Hirota T., Yamamoto S., 2008, ApJ, 672, 371

Sakai N., Sakai T., Hirota T., Yamamoto S., 2010, ApJ, 722, 1633

Sakai N. et al., 2014a, Nature, 507, 78

Sakai N. et al., 2014b, ApJ, 791, L38

Sandell G., Aspin C., Duncan W. D., Russell A. P. G., Robson E. I., 1991, ApJ, 376, L17

Sandford S. A., Nuevo M., Bera P. P., Lee T. J., 2020, Chem. Rev., 120, 4616

Santangelo G. et al., 2014, A&A, 568, A125

Santangelo G. et al., 2015, A&A, 584, A126

Sarrasin E., Abdallah D. B., Wernli M., Faure A., Cernicharo J., Lique F., 2010, MNRAS, 584, A126

Schilke P., Walmsley C. M., Pineau Des Forets G., Roueff E., Flower D. R., Guilloteau S., 1992, A&A, 256, 595

Schlafly E. F. et al., 2014, ApJ, 786, 29

Schuhmann M. et al., 2019, A&A, 630, A31

Smith K. W., Bonnell I. A., Emerson J. P., Jenness T., 2000, MNRAS, 319, 991

Snyder L. E., Buhl D., 1972, ApJ, 177, 619

Tafalla M., Myers P. C., Mardones D., Bachiller R., 2000, A&A, 359, 967

Taniguchi K., Gorai P., Tan J. C., 2023, Carbon-Chain Chemistry in the Interstellar Medium , preprint (arXiv:2303.15769)

Taquet V., López-Sepulcre A., Ceccarelli C., Neri R., Kahane C., Charnley S. B., 2015, ApJ, 804, 81

Taquet V. et al., 2020, A&A, 637, A63

Tobin J. J., Hartmann L., Calvet N., D'Alessio P., 2008, ApJ, 679, 1364

Turner A. M., Kaiser R. I., 2020, Acc. Chem. Res., 53, 2791

van Dishoeck E. F., Blake G. A., 1998, ARA&A, 36, 317

Vastel C., Ceccarelli C., Lefloch B., Bachiller R., 2014, ApJ, 795, L2

Vastel C., Bottinelli S., Caux E., Glorian J.-M., Boiziot M., 2015, in Martins F., Boissier S., Buat V., Cambrésy L., Petit P., eds, SF2A-2015: Proceedings of the Annual Meeting of the French Society of Astronomy and Astrophysics. p. 313

Watanabe N., Kouchi A., 2002, ApJ, 571, L173

Yang Y.-L. et al., 2021, ApJ, 910, 20

Yen H.-W., Takakuwa S., Ohashi N., Ho P. T. P., 2013, ApJ, 772, 22

Yoshida K., Sakai N., Nishimura Y., Tokudome T., Watanabe Y., Sakai T., Takano S., Yamamoto S., 2019, PASJ, 71, S18

Zamirri L., Ugliengo P., Ceccarelli C., Rimola A., 2019, ACS Earth Space Chem., 3, 1499

Zhu C., Turner A. M., Meinert C., Kaiser R. I., 2020, ApJ, 889, 134

SUPPORTING INFORMATION

Supplementary data are available at *MNRAS* online.

SI.pdf

Please note: Oxford University Press is not responsible for the content or functionality of any supporting materials supplied by the authors. Any queries (other than missing material) should be directed to the corresponding author for the article.

This paper has been typeset from a TEX/LATEX file prepared by the author.